

不同驱动力对熔池表面变形行为影响的数值模拟

黄 勇, 李 慧, 王新鑫, 姚宇航*

(兰州理工大学省部共建有色金属先进加工与再利用国家重点实验室, 兰州 730050)

摘 要: 基于流体动力学方程, 采用焓-孔隙度法来处理液-固相变, 采用VOF方法追踪熔池自由表面变形, 建立了固定电弧下的三维瞬态TIG焊熔池数学模型, 求解获得了在浮力、Marangoni力、电磁力和电弧压力单独作用时的熔池表面变形行为及其温度场与速度场的分布。模拟结果表明, 在大电流($I \geq 250$ A)时, 在浮力、表面张力温度系数为正时的Marangoni力、电磁力单独作用于熔池上表面将会产生凸起变形, 在电弧压力、表面张力温度系数为负时的Marangoni力单独作用下, 熔池上表面将会产生凹陷变形。在大电流下, TIG焊和活性TIG焊熔池均产生凹陷变形。TIG焊熔池的中心区域形成向内的涡流, 边缘部位形成向外的涡流, 而活性TIG熔池在熔池中心和熔池边缘则分别形成两种成因不同的内向涡流。熔池表面变形量并不是各个驱动力作用的简单叠加。

关键词: 流体体积方法; 驱动力; 表面变形; 熔池

中图分类号: TG 444 文献标识码: A 文章编号: 0253-360X(2016)08-0045-05

0 序 言

钨极惰性气体保护(TIG)焊自从出现以来, 由于它的焊缝成形好, 性能优越, 可焊接多种金属的优点, 一直被广泛应用。熔池中流体的动态行为以及温度场的分布直接影响焊缝最后的表面成形。对于TIG焊熔池的数值模拟, 国内外已经有大量的研究与成果^[1-3]。但是, 迄今为止, 国内外大多数学者都是在忽略熔池表面变形下对熔池的速度场以及温度场进行研究。陆善平等人^[4]模拟了在氩弧和氦弧下浮力、表面张力、电磁力和气体剪切力分别对熔池中流体的作用方式, 但是却忽略了电弧压力及其它熔池流体流动驱动力对自由表面变形的影响, 然而熔池流动驱动力对熔池表面的成形却有着重要的作用。Tanaka等人^[5]在考虑钨极、电弧、阳极的条件下, 建立了二维电弧熔池统一数学模型。Wany等人^[6]建立了三维双钨极电弧熔池统一模型, 并深入分析了熔池形貌的成因, 得出了阳极表面的热流分布影响熔宽, 表面张力梯度影响熔深, 而热流分布和表面张力梯度共同作用影响熔池的形状和大小, 但是却忽略了自由表面对熔池形貌的重要影响。Choo等人^[7]虽然考虑了电弧与熔池自由表面的相互作用, 但是所用的表面凹陷模型并非由计算所得, 而是通过试验数据直接给定的。雷永平等人^[8]建立了焊

接电弧与熔池的双向耦合模型, 但其只对TIG焊自由表面变形进行了简单的分析, 并没有对其做深入的研究。因此对熔池表面变形行为做进一步的研究, 不仅有助于理解熔池的表面变形的原因, 更有助于掌握熔池表面变形的一般规律。

文中以TIG焊以及活性TIG的熔池为研究对象, 利用流体体积法(volume of fluid, VOF)追踪自由表面变形, 建立三维非稳态熔池数学模型, 计算得到了不同熔池流体流动驱动力作用下的流场、温度场以及自由表面变形行为, 为揭示焊缝成形原因提供理论指导。文中是GPCA-TIG焊^[9]电弧熔池交互作用模型的前期工作。

1 数学模型

1.1 假设条件

(1) 假设熔池中的液态金属流动为层流、不可压缩的Newton流; (2) 熔池内的热源采用半椭球体体积热源分布, 电流密度分布采用平面高斯分布; (3) 除热导率和粘度外, 其余热物理常数与温度无关。

1.2 控制方程

根据以上的基本假设, 质量连续性方程、动量和能量方程的控制方程如下。

质量守恒方程为

$$\frac{\partial \rho}{\partial t} + \nabla \cdot (\rho V) = 0 \quad (1)$$

收稿日期: 2014-09-11

基金项目: 国家自然科学基金资助项目(51265029)

* 参加此项研究工作的还有陆肃中

动量守恒方程为

$$\frac{\partial(\rho u)}{\partial t} + \nabla \cdot (\rho V u) = \nabla(\mu \nabla u) - \frac{\partial p}{\partial x} + S_u \quad (2)$$

$$\frac{\partial(\rho v)}{\partial t} + \nabla \cdot (\rho V v) = \nabla(\mu \nabla v) - \frac{\partial p}{\partial y} + S_v \quad (3)$$

$$\frac{\partial(\rho w)}{\partial t} + \nabla \cdot (\rho V w) = \nabla(\mu \nabla w) - \frac{\partial p}{\partial z} + S_w \quad (4)$$

能量守恒方程为

$$\frac{\partial(\rho T)}{\partial t} + \nabla(\rho V T) = \nabla\left(\frac{k}{c} \nabla T\right) + S_T \quad (5)$$

式中: u, v, w 分别为 x, y, z 向上的速度; μ 为粘度; p 为压力; T 为温度; S_u, S_v, S_w 分别表示 x, y, z 三个方向上的动量源项; S_T 为能量方程的源项; V 为速度; k 为热导率; c 为电压比热; ρ 为密度。

1.3 焓-孔隙度法

采用焓-孔隙度法^[10]来处理合金相变,液相体积分数的 f_1 采用线性关系,表达式为

$$f_1 = \begin{cases} 0 & T < T_s \\ \frac{T - T_s}{T_1 - T_s} & T_s \leq T \leq T_1 \\ 1 & T > T_1 \end{cases} \quad (6)$$

式中: T 为温度; T_s 为固相线温度; T_1 为液相线温度。

1.4 自由表面追踪

在熔池与电弧相互作用的表面,采用流体体积 (VOF) 法^[11]来追踪熔池表面液相体积分数的变化,并且用函数 $F(x, y, z)$ 来表示三维坐标下单元网格内流体所占的体积分,并且满足以下方程,即

$$\frac{\partial F}{\partial t} + u \frac{\partial F}{\partial x} + v \frac{\partial F}{\partial y} + w \frac{\partial F}{\partial z} = 0 \quad (7)$$

式中: F 为计算区域内单元网格中流体的平均体积分。当 $F=0$ 时,则该单元网格中没有金属;当 $F=1$ 时,则该单元网格中全部都是金属;当 $0 < F < 1$ 时,则该单元网格中既存在金属也存在气相。

1.5 边界条件

(1) 作用于熔池自由表面的压力包括电弧压力和表面张力压力,即^[11]

$$p = p_{\text{arc}} + \gamma \kappa \quad (8)$$

式中: p 为垂直作用于熔池自由表面的总压力; γ 为表面张力系数; κ 为自由表面的曲率; p_{arc} 为电弧压力。电弧压力^[12]为

$$p_{\text{arc}} = \frac{\mu_0 I^2}{8\pi^2 (\sigma_x + \sigma_y)^2} \exp\left(-\frac{(x+y)^2}{2(\sigma_x + \sigma_y)^2}\right) \quad (9)$$

式中: μ_0 为真空磁导率; I 为电流; σ_x, σ_y 为电流分布参数。

$$\kappa = -\left[\nabla\left(\frac{\mathbf{n}}{|\mathbf{n}|}\right)\right] = \frac{1}{|\mathbf{n}|} \left[\left(\frac{\mathbf{n}}{|\mathbf{n}|} \cdot \nabla\right) |\mathbf{n}| - (\nabla \cdot \mathbf{n}) \right] \quad (10)$$

式中: \mathbf{n} 为垂直于自由表面的法向量,其值为在单元网格 x, y, z 方向上的体积分的梯度。即:

$$\mathbf{n} = \nabla F = \frac{\partial F}{\partial x} \mathbf{i} + \frac{\partial F}{\partial y} \mathbf{j} + \frac{\partial F}{\partial z} \mathbf{k} \quad (11)$$

(2) 作用于熔池自由表面的切向力为 Marangoni 切应力,即:

$$\tau_{Mx} = \frac{\partial \gamma \partial T}{\partial T \partial x} \quad (12)$$

$$\tau_{My} = \frac{\partial \gamma \partial T}{\partial T \partial y} \quad (13)$$

Marangoni 力在 z 方向求导,将表面力转化为体积力加载在源项 S_u 和 S_v 中。

$$\frac{\partial \tau_{Mx}}{\partial z} = \frac{\partial}{\partial z} \left(\frac{\partial \gamma \partial T}{\partial T \partial x} \right) \quad (14)$$

$$\frac{\partial \tau_{My}}{\partial z} = \frac{\partial}{\partial z} \left(\frac{\partial \gamma \partial T}{\partial T \partial y} \right) \quad (15)$$

(3) xz 中心对称面 ($y=0$) 与 yz 中心对称面 ($x=0$)。

$$\frac{\partial T}{\partial x} = 0 \quad \frac{\partial v}{\partial x} = 0 \quad \frac{\partial w}{\partial x} = 0 \quad u = 0 \quad (16)$$

$$\frac{\partial T}{\partial y} = 0 \quad \frac{\partial u}{\partial y} = 0 \quad \frac{\partial w}{\partial y} = 0 \quad v = 0 \quad (17)$$

1.6 体积热源

假设在整个求解区域,体积热源只作用在金属区域,热流密度服从半椭球体热源分布^[13],即

$$q(x, y, z) = \frac{6\sqrt{3}Q}{a_h b_h c_h \pi \sqrt{\pi}} \exp\left(-\frac{3x^2}{a_h^2} - \frac{3y^2}{b_h^2} - \frac{3z^2}{c_h^2}\right) \quad (18)$$

式中: Q 为电弧有效热功率; a_h, b_h, c_h 为体积热源的热流分布参数,其值分别为 0.004 5, 0.004 5, 0.000 5 m。

1.7 电磁力

由于电流密度服从高斯分布,所以 x, y, z 动量源项如下所示^[13]。

$$(\mathbf{J} \times \mathbf{B})_x = -\frac{\mu_0 I^2}{4\pi^2 \sigma_j^2 r} \exp\left(-\frac{r^2}{2\sigma_j^2}\right) \left[1 - \exp\left(-\frac{r^2}{2\sigma_j^2}\right)\right] \left(1 - \frac{z}{L_z}\right)^2 \frac{x}{r} \quad (19)$$

$$(\mathbf{J} \times \mathbf{B})_y = -\frac{\mu_0 I^2}{4\pi^2 \sigma_j^2 r} \exp\left(-\frac{r^2}{2\sigma_j^2}\right) \left[1 - \exp\left(-\frac{r^2}{2\sigma_j^2}\right)\right] \left(1 - \frac{z}{L_z}\right)^2 \frac{y}{r} \quad (20)$$

$$(\mathbf{J} \times \mathbf{B})_z = \frac{\mu_0 I^2}{4\pi^2 L_z r^2} \left[1 - \exp\left(-\frac{r^2}{2\sigma_j^2}\right)\right]^2 \left(1 - \frac{z}{L_z}\right) \quad (21)$$

式中: σ_j 为电流分布参数; L_z 为焊件厚度。

2 数值方法

对焊接过程中的熔池传热与流动过程进行数值

模拟,采用 PISO 算法对压力进行二次修正,并利用流体软件 FLUENT6.3.2 编制用户子程序进行二次开发,将所编写的公式通过源项或边界条件加入到软件相应的数据接口.由于 Courant number 大小的限制,计算中的时间步长设为 10^{-5} s.

3 计算结果与比较

文中采用 SUS304 不锈钢为研究对象,模拟其定点 TIG 焊,母材的大小为 $20\text{ mm} \times 20\text{ mm} \times 8\text{ mm}$,其它热物性参数见参考文献 [13],焊接电流为 250 A,电弧电压为 14 V 时,对熔池的温度场与流场进行模拟与分析.

3.1 浮力

从图 1 发现,在只有浮力作用的熔池中,最大速度约为 0.011 m/s ,出现在近熔池上表面的边缘区域,并且在熔池中形成了向外的涡流,熔池表面变形量 Δx 均大于零(由于 VOF 计算方法在计算界面曲率误差较大^[14],在小变形下这种误差更为明显,导致计算中的自由表面变形单一,并且计算所得的熔融金属的速度量级的大小以及流动方向规律与文献 [4] 观点一致),熔池表面凸起,最大变形量为 $+0.144\text{ mm}$ (以试样的初始平面为基准,“+”代表变形高于初始平面,凸起;“-”代表变形低于初始平面,凹陷).

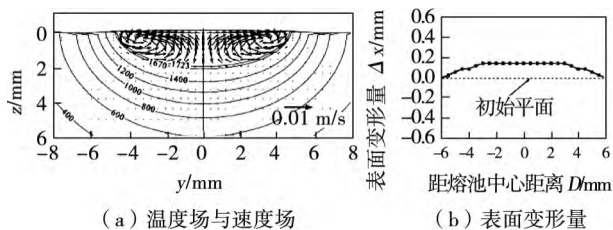


图 1 浮力作用下的熔池
Fig. 1 Weld pool under buoyancy

3.2 电弧压力

图 2 为电弧压力单独作用在焊接熔池中的速度场和温度场及熔池表面变形量,最大变形量为 -0.156 mm . 电弧压力的作用比较复杂.一方面当电弧压力作用在熔池表面时,先使熔池中熔化的部分产生向下的凹陷,同时又产生了向下的速度,而恰是向下的速度带走了熔池上表面的熔融金属,使熔池的凹陷变形增加,而又因为电弧压力是垂直作用在熔池自由表面上,使得在熔池边缘产生向外的流动,并且在熔池的边缘区域形成了一个向外的涡流;在熔池的中心区域形成向内的涡流.而另一方面则

是熔池上部的体积流量变化产生.最大速度在熔池中心区域,并沿着边缘的方向,速度逐渐减小.且越接近熔池的底部,熔池的速度越小.从边缘带入熔池上部的熔融金属的量要少于带出的量,使得熔池上部的熔融金属减少.基于这两方面的原因,熔池上部的熔融金属被边缘向外和向下的速度场带走,从而熔池中心区域出现凹陷.

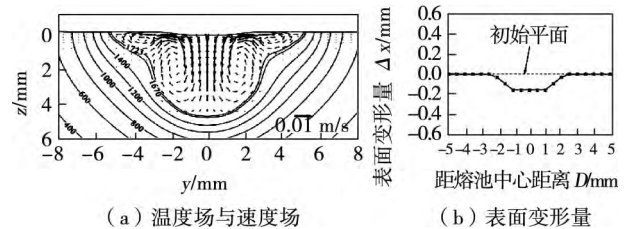


图 2 电弧压力作用下的熔池
Fig. 2 Weld pool under arc pressure

3.3 电磁力

从图 3 中可以发现在熔池中出现两个完整的向内的涡流,并且熔池上表面微微凸起,熔池表面最大变形量为 $+0.053\text{ mm}$.在 $z = 0\text{ mm}$ 时,最大速度分布在熔池中心两侧,为 0.12 m/s .随着距熔池上表面的距离的增加,熔池最大速度均出现在熔池的中心,且呈先增大后减小的趋势.在此过程中最大速度约为 0.22 m/s ,位置在 $z > 2\text{ mm}$ 处.由于熔池内的流场是向内流动的,这样的流动将熔池边缘的熔融金属带到了熔池中央,而熔池中所存在的向下的流动又将熔池上表面的熔融金属带到熔池底部.由于熔池中的最大速度在 $z = 2\text{ mm}$ 左右,并且熔池上表面的速度也比较大,所以从熔池边缘带到中心的熔融金属比带到熔池底部的多,所以熔池上表面凸起.

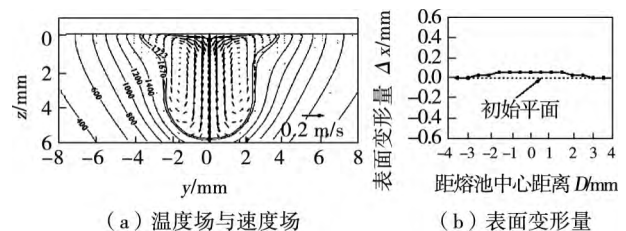


图 3 电磁力作用下的熔池
Fig. 3 Weld pool under electromagnetic force

3.4 负的表面张力温度系数

图 4a 为在 $\partial\gamma/\partial T = -1.2 \times 10^{-4}$ 时的 Marangoni 驱动力单独作用在熔池中所产生的温度场与速度场.整个熔池的形貌为扁平状,熔池中形成两个向

外的涡流,且最大速度出现在熔池上表面附近.熔池表面变形量如图4b所示,最大变形量为 -0.208 mm .由于熔池中只有 Marangoni 力的作用,熔池中心的速度比较小,热对流的效果并不明显,电弧产生的热量并未有效的散失,导致熔池中心的热量积累,使得熔池中心的熔池底部向下凹陷.

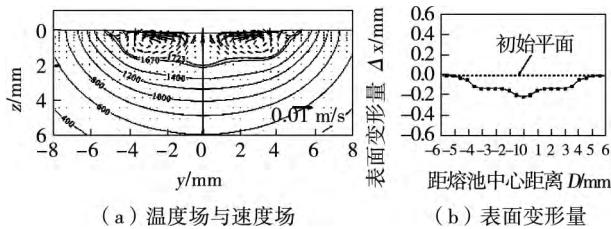


图4 $\partial\gamma/\partial T < 0$ 时 Marangoni 力作用下的熔池
Fig. 4 Weld pool under Marangoni force ($\partial\gamma/\partial T < 0$)

3.5 正的表面张力温度系数

图5a为 $\partial\gamma/\partial T = 1.2 \times 10^{-4}$ 时的 Marangoni 驱动力单独作用在熔池中所产生的温度场与速度场.熔池表面有微量的凸起,变形量如图5b所示,最大变形量为 0.071 mm .可以发现,熔池中形成了两个强度较大的向内的涡流,且与电磁力单独作用时相比较,Marangoni 力在熔池上表面产生的速度约为 0.21 m/s ,比单独电磁力作用时大 0.1 m/s ,而在熔池中心处的最大速度约为 0.22 m/s ,两者相差不大.由于这种速度场的分布,流入熔池上部金属的体积流量与流向熔池底部的体积流量几乎相同,但流入熔池上部的体积流量较多,以至于在只有 Marangoni 力的时候,熔池上表面只有微量的凸起变形.

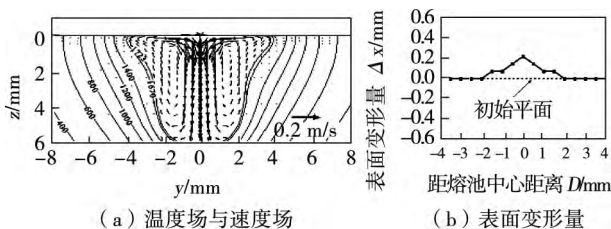


图5 $\partial\gamma/\partial T > 0$ 时 Marangoni 力作用下的熔池
Fig. 5 Weld pool under Marangoni force ($\partial\gamma/\partial T > 0$)

3.6 综合作用

图6a为 250 A 下TIG焊熔池的温度场与速度场.从图6中可以发现,在熔池的中心区域形成向内的涡流,在熔池的边缘部位则形成向外的涡流.向内的涡流把电弧热带到了熔池底部,起到挖掘作用.而向外的涡流则是将电弧热带到了熔池边缘,增加了熔宽.熔池表面产生凹陷,变形量如图6b所示.

最大变形量为 0.140 mm ,分布在熔池边缘附近.

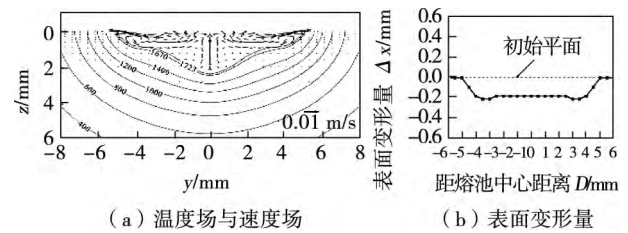


图6 TIG 焊熔池
Fig. 6 Weld pool under TIG welding

图7a为 250 A 下活性TIG焊熔池的温度场与速度场.可以明显看出,在整个熔池中形成了两种向内的涡流,一种是在熔池的中部形成一个完整向内的涡流,这主要是由电磁力的作用;而另一种则是分布在近熔池表面的边缘部位,这种涡流的形成则主要是被电弧压力削减后的 Marangoni 力的作用.图7b为活性TIG焊熔池表面变形量的分布图,最大变形量为 0.227 mm .

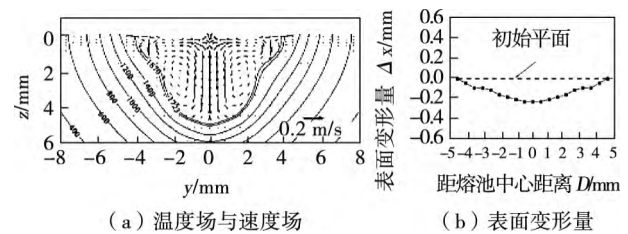


图7 活性TIG焊熔池
Fig. 7 Weld pool under activated TIG welding

通过测量 250 A 下TIG焊熔池表面的变形量为 -0.140 mm ,活性TIG焊熔池表面的变形量为 -0.227 mm .从变形量可以得知,TIG焊与活性TIG焊中的驱动力均是浮力、电弧压力、电磁力和 Marangoni 力的综合作用,而它们各自单独作用时的变形量为 $+0.144\text{ mm}$ 、 -0.156 mm 、 $+0.053\text{ mm}$ 、 -0.208 mm ($\partial\gamma/\partial T < 0$), $+0.071\text{ mm}$ ($\partial\gamma/\partial T > 0$), 总和分别为 -0.167 mm 和 -0.112 mm ,这些值与TIG焊与活性TIG焊的变形量并不相同.由此可得,熔池表面变形量的大小并不是各个驱动力的简单叠加,其中的相互作用还很复杂,需要进一步深入研究.

4 结 论

(1) 在浮力、 $\partial\gamma/\partial T > 0$ 时的 Marangoni 力、电磁力单独作用于熔池上表面将会产生凸起变形,在电

弧压力、 $\partial\gamma/\partial T < 0$ 时的 Marangoni 力单独作用下, 熔池上表面将会产生凹陷变形。

(2) 大电流下 TIG 焊熔池的中心区域形成向内的涡流, 在熔池的边缘部位则形成向外的涡流; 在活性 TIG 熔池中由于 Marangoni 力和电磁力的作用分别在熔池中心和熔池边缘形成了两种不同成因的内向涡流。

(3) 熔池上部的体流量的变化是熔池上部熔融金属是否积累的原因, 而不同熔池流动驱动力将影响熔池最大流速产生的位置, 间接影响着熔池上表面的凹陷或凸起。

(4) 熔池表面变形量的大小, 并不是各个驱动力作用的简单叠加。

参考文献:

- [1] Oreper G M, Szekely. Heat and fluid flow phenomena in weld pools[J]. *Journal of Fluid Mechanics*, 1984, 147(10): 53 - 79.
- [2] Zacharia T, David S A, Vitek J M, *et al.* Computational modeling stationary gas-tungsten-arc weld pools and comparison to stainless steel-304 experimental results[J]. *Metallurgical Transactions B-Process Metallurgy*, 1991, 22(2): 243 - 257.
- [3] Choo R T C, Szekely J, David S A. On the calculation of the free surface temperature of gas-tungsten-arc weld pools from first principles: Part II-modeling the weld pool and comparison with experiments [J]. *Metallurgical Transactions B-Process Metallurgy*, 1992, 23(3): 371 - 378.
- [4] 陆善平, 董文超, 李殿忠, 等. 电弧特性及其对熔池形貌影响的数值模拟[J]. *物理学报*, 2009, 58: S94 - S103.
Lu Shanping, Dong Wenchao, Li Dianzhong, *et al.* Numerical simulation of arc properties and their effects on the weld shape[J]. *Acta Physica Sinica*, 2009, 58(Z1): S94 - S103.
- [5] Tanaka M, Terasaki H, Ushi M, *et al.* A unified numerical modeling of stationary tungsten-inert-gas welding process[J]. *Metallurgical & Materials Transactions A*, 2001, 33(7): 2043 - 2052.
- [6] Wang X X, Fan D, Huang J K, *et al.* A unified model of coupled arc plasma and weld pool for double electrodes TIG welding [J]. *Journal of Physics D: Applied Physics*, 2014, 47(27): 275202 - 275215.
- [7] Choo R T C, Szekely J, Westhoff R C. Modeling of high-current arcs with emphasis on free surface [J]. *Welding Journal*, 1990, 69(9): 346s - 361s.
- [8] 雷永平, 顾向华, 史耀武, 等. GTA 焊接电弧与熔池系统的双向耦合数值模拟[J]. *金属学报*, 2001, 37(5): 537 - 542.
Lei Yongping, Gu Xianghua, Shi Yaowu, *et al.* Numerical analysis of the two-way interaction between a mutually coupled weld-pool and weld-arc for GTA welding process [J]. *Acta Physica Sinica*, 2001, 37(5): 537 - 542.
- [9] 黄 勇, 刘瑞琳, 樊 丁, 等. 气体熔池耦合活性 TIG 焊方法[J]. *焊接学报*, 2012, 33(9): 13 - 16.
Huang Yong, Liu Ruilin, Fan Ding, *et al.* Gas pool coupled activating TIG welding method [J]. *Transactions of the China Welding Institution*, 2012, 33(9): 13 - 16.
- [10] Voller V R, Prakash C. A fixed grid numerical modeling methodology for convection-diffusion mushy region phase-change problems [J]. *International Journal of Heat Mass Transfer*, 1987, 30(8): 1709 - 1719.
- [11] Hirt C W, Nichols B D. Volume of Fluid (VOF) method for the dynamics of free boundaries [J]. *Journal of Computational Physics*, 1981, 39(1): 201 - 225.
- [12] Kothe D B, Mjolsness R C. A new model for incompressible flows with free surfaces [J]. *American Institute of Aeronautics and Astronautics*, 1992, 30(11): 2694 - 2700.
- [13] 武传松. 焊接热过程与熔池形态 [M]. 北京: 机械工业出版社, 2008.
- [14] 叶政钦, 刘启鹏, 李星红, 等. 复杂两相流中界面追踪方法—VOSET 的性能分析 [J]. *化工学报*, 2011, 62(6): 1524 - 1530.
Ye Zhengqin, Liu Qipeng, Li Xinghong, *et al.* Performance analysis of interface tracking method for complex two-phase flows—VOSET [J]. *CIESC Journal*, 2011, 62(6): 1524 - 1530.

作者简介: 黄 勇 男, 1972 年出生, 教授, 博士。主要从事高效焊接技术研究。发表论文 70 余篇。Email: hyorhot@lut.cn

GAO Jian , CHEN Hui (School of Materials Science and Engineering , Southwest Jiaotong University , Chengdu 610031 , China) . pp 39-44

Abstract: High frequency pulses (HFPs) power source were parallelly connected with the power source of single-pulse mode MIG arc , which are applied to laser-MIG hybrid welding. The cladding on A7N01 aluminum alloy was executed to investigate the dynamics of droplet transfer and arc with the effects of coupled HFPs through high speed camera observation. The shaping-characteristic and microstructure of cladding layer were also studied by metallographic analysis. The results show that the arc length and voltage increase after HFPs being coupled. The base current of single pulse MIG arc decreases , while the peak current has little changes compared with that without HFPs coupling. In conventional laser-MIG hybrid welding , the droplets are partly transferred as meso-spray mode. The finger-penetration weld can be obtained , which probably causing defects in the weld root. After HFPs being coupled , partly meso-spray transfer changes to completely spray transfer. The surface of cladding layer becomes smoother with the disappearance of fish-scale pattern and finger-penetration depth. Although the grain size has no significant changes , the size of second phase particles becomes smaller and more uniformly distributed in grains as strengthened phase.

Key words: aluminum alloy; laser-MIG hybrid welding; high frequency pulses; droplet transfer; arc ultrasonic

Numerical simulation of effects of different driving force on surface deformation of weld pool HUANG Yong , LI Hui , WANG Xinxin , YAO Yuhang , LU Suzhong(State Key Laboratory of Advanced Processing and Recycling of Non-ferrous Metals , Lanzhou University of Technology , Lanzhou 730050 , China) . pp 45-49

Abstract: A three-dimensional transient mathematical model of weld pool for a stationary tungsten inert gas welding was established based on the fluid dynamic equations . In this model , enthalpy-porosity method was used to handle liquid-solid phase change , VOF method was employed to track the free surface deformation of the weld pool. By solving these equations , the deformation behavior of surface and the distributions of temperature and velocity were obtained under the independent action by buoyancy , Marangoni force , electromagnetic force and arc pressure , respectively. The results indicate that at high welding current ($I \geq 250$ A) , a surface projection forms in weld pool when buoyancy , Marangoni force with positive temperature coefficient of surface tension and electromagnetic force were acted independently , while a surface depression forms under the action of arc pressure , Marangoni force with negative temperature coefficient of surface tension. At high welding current , weld pool depression phenomenon appears for both TIG welding and activated flux TIG welding. For TIG welding , there exists an inward vortex in the central zone of the weld pool , while a outward vortex appears in the periphery. For activated flux TIG welding , two inward vortexes are induced by different factors in the central zone and periphery of the weld pool , respectively. The magnitude of surface deformation was not superimposed simply by each driving force.

Key words: VOF method; driving force; surface deformation; weld pool

Torque feature in bobbin tool FSW of 6061 aluminum alloy

CHEN Shujin , CAO Fujun , LIU Bin , HU Xiaoqing , LI Hao , XUE Junrong (Jiangsu University of Science and Technology , Zhenjiang 212003 , China) . pp 50-54

Abstract: To investigate the torque characteristics in bobbin tool friction stir welding (BTFSW) of 6061 aluminum alloy ,

the torque in BTFSW was measured , the frequency spectrum and the peak of torque were analyzed , and then the relationship between the torque oscillation and the surface shape of welded joint was also discussed. The research indicates that the torque in BTFSW is periodic. The major frequency of the torque is close to 2 times of the spindle frequency. The frequency difference illustrates that the stacking behavior exists between the tool and the metal flow at different velocity. The experimental results indicated that the peak of torque increases with welding speed being increased and decreases with rotation speed being increased when interface temperature of tool and workpiece was lower than 500 °C . Smaller torque oscillation will not affect the surface shape of welded joint , but if the interface temperature was higher than 550 °C , the torque will appear abnormal oscillation under adverse condition , such as the too short distance between top and back shoulders , slow travel speed , high rotation speed. This research will be useful to indicate the mechanism of BTFSW , 3-D force characteristics and the relationship between welding parameters and welding quality.

Key words: bobbin tool friction stir welding; welding torque; spectrum analysis; weld surface

Measuring residual stress of chain based on the method of digital image correlation LIN Liexiong¹ , LU Hao^{1,2} , XU Jijin¹ , CHENG Zhewen¹ (1. School of Materials Science and Engineering , Shanghai Jiao Tong University , Shanghai 200240 , China; 2. Shanghai Key Laboratory of Materials Laser Processing and Modification , Shanghai Jiao Tong University , Shanghai 200240 , China) . pp 55-58

Abstract: A stress measurement system was built based on digital image correlation method. The influence of speckle pattern quality on the measurement accuracy was analyzed , and the accuracy of this measurement system was verified through in-plane translation and the test of plane stress state. The results show that the measurement accuracy can be improved with the increase of the quality of speckle pattern to a certain extent. All the relative errors in the test of in-plane translation were less than 3.5% , which indicate that the system has high accuracy. When this measurement system was used to measure the welding residual stress of the chain , the results are basically the same with that from strain gauges. It's worth noting that , this stress measurement system has advantages such as simple operation and high accuracy , which can be used to measure the residual stress instead of strain gauge under certain conditions.

Key words: digital image correlation; welding residual stress; in-plane translation; plane stress; chain

Crystal orientation evolution of friction stir welding of 2024/7075 dissimilar aluminum alloys ZHOU Jun^{1,2} , ZHANG Jin^{1,2} , JI Pengfei^{1,2} (1. Institute for Advanced Materials Technology , University of Science and Technology Beijing , Beijing 100083 , China; 2. Beijing Key Lab for Corrosion , Erosion and Surface Technology , University of Science and Technology Beijing , Beijing 100083 , China) . pp 59-62

Abstract: The optical microscope and electron back scattering diffraction(EBSD) were used to comparative study the microstructure features , grain boundary characteristics and the evolution of the texture in friction stir welded joint and base metal of 2024/7075 dissimilar aluminum alloys. The results show that the content of low angle grain boundary in thermal mechanical affected zone at retreating side grain is significantly higher than that of the base metal , but there is no obvious change at advancing side. Dynamic recrystallization occurs in stir zone , and the content of high angle grain boundary increases significantly. 2024 aluminum alloy at retreating side has a weak orientation. 7075